The Astronomical Journal, 161:295 (16pp), 2021 June https://doi.org/10.3847/1538-3881/abf9a8

Observations with the Differential Speckle Survey Instrument. X. Preliminary Orbits of K-dwarf Binaries and Other Stars

Elliott P. Horch[1,9], Kyle G. Broderick[1,10], Dana I. Casetti-Dinescu[1], Todd J. Henry[2], Francis C. Fekel[3,11], Matthew W. Muterspaugh[4], Daryl W. Willmarth[5], Jennifer G. Winters[6,11], Gerard T. van Belle[7,11], Catherine A. Clark[7,8,12], and Mark E. Everett[5]
[1] Department of Physics, Southern Connecticut State University, 501 Crescent Street, New Haven, CT 06515, USA; horche2@southernct.edu
[2] RECONS Institute, Chambersburg, PA 17201, USA
[3] Center of Excellence in Information Systems, Tennessee State University, 3500 John A. Merritt Boulevard, Box 9501, Nashville, TN 37209, USA
[4] Columbia State Community College, 1665 Hampshire Pike, Columbia, TN 38401, USA
[5] NSF's National Optical-Infrared Research Laboratory, 950 N. Cherry Avenue, Tucson, AZ 85719, USA
[6] Center for Astrophysics, Harvard & Smithsonian, 60 Garden Street, Cambridge, MA 02138, USA
[7] Lowell Observatory, 1400 West Mars Hill Road, Flagstaff, AZ 86001, USA
[8] Department of Astronomy and Planetary Science, Northern Arizona University, Flagstaff, AZ 86001, USA
Received 2021 March 21; revised 2021 April 13; accepted 2021 April 15; published 2021 June 3

Abstract

This paper details speckle observations of binary stars taken at the Lowell Discovery Telescope, the WIYN telescope, and the Gemini telescopes between 2016 January and 2019 September. The observations taken at Gemini and Lowell were done with the Differential Speckle Survey Instrument (DSSI), and those done at WIYN were taken with the successor instrument to DSSI at that site, the NN-EXPLORE Exoplanet Star and Speckle Imager (NESSI). In total, we present 378 observations of 178 systems, and we show that the uncertainty in the measurement precision for the combined data set is ∼2 mas in separation, ∼1°–2° in position angle depending on the separation, and ∼0.1 mag in magnitude difference. Together with data already in the literature, these new results permit 25 visual orbits and one spectroscopic-visual orbit to be calculated for the first time. In the case of the spectroscopic-visual analysis, which is done on the ternary star HD 173093, we calculate masses with a precision of better than 1% for all three stars in that system. Twenty-one of the visual orbits calculated have a K dwarf as the primary star; we add these to the known orbits of K-dwarf primary stars and discuss the basic orbital properties of these stars at this stage. Although incomplete, the data that exist so far indicate that binaries with K-dwarf primaries tend not to have low-eccentricity orbits at separations of one to a few tens of astronomical units, that is, on solar system scales.

Unified Astronomy Thesaurus concepts: Visual binary stars (1777); Spectroscopic binary stars (1557); Interferometric binary stars (806); Speckle interferometry (1552); K dwarf stars (876)

Supporting material: machine-readable tables

1. Introduction

While there have been comprehensive multiplicity studies of G and M dwarfs, K dwarfs have remained somewhat neglected observationally. Duchêne & Kraus (2013) gave a thorough review of stellar multiplicity from formation mechanisms to observational statistics, yet K dwarfs were not discussed, due to the relative lack of data available at the time compared with other spectral types. Yet, what we know observationally about G and M dwarfs motivates a careful study of K dwarfs even from the perspective of the most basic statistics. The G-dwarf multiplicity rate has been well established to be about 50% nonsingle (Duquennoy & Mayor 1991; Raghavan et al. 2010), and more recent work by Winters et al. (2019) indicates that M dwarfs have a much lower multiplicity rate, roughly half that of G dwarfs, so that a study of K dwarfs will allow us to see at what mass this transition occurs and how sharp it is. K-dwarf stars are also important for exoplanet research, as they are approximate analogs to our Sun in important ways. Because K dwarfs are roughly twice as common as G dwarfs, in a volume-limited sample they provide a larger set of stars that can be analyzed in statistical studies to reveal clues about star and planet formation history. In addition, large subsets of stars can be sensibly subdivided to learn more about parameters that may influence the formation outcomes, such as age, metallicity, and magnetic properties. Unlike M dwarfs, they are relatively bright and easily observed in a survey capacity at 4 m class telescopes. At the same time, they represent a more favorable situation in terms of observational ease in detecting transit signals compared to G dwarfs and offer shorter orbital periods for exoplanets that are in their habitable zones.

For these reasons, since 2015, our collaboration has been working to provide the same kind of volume-complete, unbiased statistics for K dwarfs that exist for the other lower-mass spectral types on the main sequence. This is being accomplished with a combination of three separate surveys that together span the complete range of separations for gravitationally bound companions. First, we are surveying nearby K stars with spectroscopy, identifying spectroscopic binaries (Paredes et al. 2021). Second, we are completing a wide-field survey using catalogs such as Gaia DR2 (Gaia Collaboration 2018) and EDR3 (Gaia Collaboration et al. 2021). Third, to bridge the separation

[9] Adjunct Astronomer, Lowell Observatory; Visiting Astronomer, Kitt Peak National Observatory; Visiting Astronomer, Gemini Observatory.
[10] Current Address: Aerospace/Hydrospace Engineering & Physical Sciences, Fairchild Wheeler Interdistrict Magnet Campus, 840 Old Town Road, Bridgeport, CT, 06606.
[11] Visiting Astronomer, Kitt Peak National Observatory.
[12] Visiting Astronomer, Gemini Observatory.

Table 1
Observing Runs

Run	Dates	Telescope	Instrument	Number of Obs.
1	2016 Jan 13–19	Gemini-N	DSSI	6
2	2016 Jan 27–28	LDT	DSSI	18
3	2016 Nov 11	WIYN	NESSI	1
4	2017 May 4–8	LDT	DSSI	46
5	2017 Jun 9–11	Gemini-S	DSSI	6
6	2017 Oct 18–21	LDT	DSSI	16
7	2018 Jan 28–Feb 1	LDT	DSSI	53
8	2018 Aug 27	LDT	DSSI	21
9	2019 Jan 18–19, 21, 25	WIYN	NESSI	134
10	2019 Sep 11–12	LDT	DSSI	77

regimes between these two surveys, we are observing the same list of stars using speckle imaging at a combination of facilities, including both Gemini telescopes, the WIYN telescope, and the Lowell Discovery Telescope (LDT). This paper presents results from the speckle survey on measurements of the companions of K-dwarf stars and some other targets of interest, and uses that information together with previous measures to derive visual orbital elements for 26 systems in all, 21 of which are K dwarfs. This brings the total number of visual orbits for systems that have a K-dwarf primary to 246; thus, this paper increases the sample by approximately 9%.

2. Observations and Data Reduction

The results presented here are derived from observing runs that took place at the LDT, WIYN, and the two Gemini telescopes from 2016 through 2019. The Differential Speckle Survey Instrument (DSSI) was used at the LDT for the majority of the observations (Horch et al. 2009). We then supplemented this data set with a run at the WIYN telescope with the NESSI speckle camera (Scott et al. 2018) in 2019, two nights of which were provided via Director's Discretionary Time. A few further observations taken at Gemini-S in 2017 June and at Gemini-N in 2016 January are also included that bear directly on the orbit calculations presented later in this paper. We have obtained a large number of observations for the program from both the WIYN and Gemini telescopes; some other Gemini measures are included in Henry et al. (2020), but the majority of our Gemini and WIYN queue observations obtained to date will be published in a future paper. In the current paper, we seek to focus primarily on objects where some previous observations exist so that orbits can be calculated either now or in the near future. A short table of the observing runs and instrument combinations in the current data set is given in Table 1.

2.1. Observational Routine

Observations were taken using the same techniques as detailed in earlier papers in this series. Specifically, objects in the target list were ordered in R.A. and then put into small groups at similar declinations. An unresolved bright star was chosen as a point source calibration object for each group from the Bright Star Catalog (Hoffleit & Jaschek 1982).

Once observations began on a given night, the telescope was kept close to the meridian to minimize residual atmospheric dispersion, and objects were observed quickly, usually with a cadence of approximately 2–10 minutes on each target, depending on its brightness. Speckle data frames are taken at a standard exposure time of 40 ms at the LDT and at WIYN, and 60 ms at Gemini. Data files are stored in 1000-frame stacks in FITS format. For fainter objects, three to five separate data files were taken prior to moving on to the next object. Because both the DSSI and NESSI speckle cameras take data in two different filters simultaneously, two such data files are produced per 1000-frame sequence.

2.2. Data Reduction

To reduce the data, the methodology remains the same as in Paper II of this series (Horch et al. 2011), where the diffraction-limited Fourier transform of object intensity distribution is assembled in the Fourier domain, low-pass filtered to reduce noise, and inverse transformed. The modulus of this function is calculated separately from its phase. The former is derived by computing the autocorrelation of each data frame, summing these, and Fourier transforming. This results in the spatial-frequency power spectrum of the image frames. To arrive at the diffraction-limited modulus, it is divided by the power spectrum of the point source calibration object and then the square root is taken. For the phase, we compute subplanes of the image bispectrum following the standard method found in Lohmann et al. (1983). Using these subplanes, we derive the phase from them using the relaxation technique of Meng et al. (1990).

Secondary stars for our systems are identified visually using the reconstructed images produced. The pixel coordinate of the peak of the secondary is used as the starting point for the fitting of interference fringes in the power spectrum using a downhill simplex algorithm. This is described more fully in Horch et al. (1996). The power spectrum fitting results in the position angle, separation, and magnitude difference of the pair.

2.3. Pixel Scale and Orientation

The pixel scale determination at all telescopes represented in Table 1 was carried out using a small group of calibration binary stars, that is, binaries with extremely well-known orbital elements, usually determined with a preponderance of data from long-baseline optical interferometry (LBOI) observations. A sequential list of the objects, observation dates, and orbits used for this purpose is shown in Table 2. Generally, this yielded results that were uncertain in terms of the scale at the $\sim$0.3% level, and for the offset angle between celestial coordinates and the pixel axes, the precision was approximately $\sim 0\overset{\circ}{.}2$.

3. Results

Our final table of results obtained using the methods above is shown in Table 3. The columns give (1) the Washington Double Star (WDS) number (Mason et al. 2001),[13] which also gives the R.A. and decl. for the object in J2000.0 coordinates; (2) an identifier from a standard star catalog, usually the Bright Star Catalog (i.e., Harvard Revised [HR]) number, the Henry Draper Catalog (HD) number, or the Durchmusterung (DM) number of the object; (3) the discoverer designation; (4) the Hipparcos Catalog number; (5) the Julian year of the observation; (6) the position angle (θ) of the secondary star relative to the primary, with north through east defining the positive sense of θ; (7) the separation of the two stars (ρ), in

[13] http://astro.gsu.edu/wds/

Table 2
Orbits and Residuals Used in the Scale Determinations

Run	WDS	Discoverer Designation	HIP	Julian Year	$\Delta\theta_A$ (°)	$\Delta\rho_A$ (mas)	$\Delta\theta_B$ (°)	$\Delta\rho_B$ (mas)	Orbit Reference
1	04136+0743	A 1938	19719	2016.0324	+0.1	−0.1	+0.1	−0.1	Muterspaugh et al. (2010)
				2016.0431	−0.1	−0.4	−0.1	−0.3	
1	22409+1433	HO 296AB	111974	2016.0349	0.0	−0.3	−0.1	−0.2	Muterspaugh et al. (2010)
				2016.0431	0.0	+0.9	−0.1	+0.7	
2	13100+1732	STF 1728AB	64241	2016.0704	+0.0	+0.0	+0.0	+0.0	Muterspaugh et al. (2015)
3	04136+0743	A 1938	19719	2016.8567	+0.1	−0.4	+0.0	+0.1	Muterspaugh et al. (2010)
3	21145+1000	STT 535AB	104858	2016.8560	−0.1	+0.4	+0.0	−0.1	Muterspaugh et al. (2008)
4	13100+1732	STF 1728AB	64241	2017.3410	+0.2	−2.4	+0.1	−1.4	Muterspaugh et al. (2015)
				2017.3463	+0.2	+3.0	+0.2	+2.5	
4	15232+3017	STF 1937AB	75312	2017.3413	+0.2	−0.8	+0.1	−0.2	Muterspaugh et al. (2010)
4	15278+2906	JEF 1	75695	2017.3413	+0.0	+0.1	+0.0	+0.1	Muterspaugh et al. (2010)
4	17080+3556	HU 1176AB	83838	2017.3414	−0.6	+0.2	−0.4	−0.9	Muterspaugh et al. (2010)
5	18384–0312	A 88AB	91394	2017.4312	−0.6	−3.2	−0.6	−2.8	Griffin (2013)
5	19026–2953	HDO 150AB	93506	2017.4395	+0.7	+3.0	+0.5	+3.0	DeRosa et al. (2011)
6	21145+1000	STT 535AB	104858	2017.7951	0.0	−0.1	0.0	−0.2	Muterspaugh et al. (2008)
6	22409+1433	HO 296AB	111974	2017.7952	0.0	+0.1	0.0	+0.2	Muterspaugh et al. (2010)
7	04136+0743	A 1938	19719	2018.0825	0.0	0.0	0.0	0.0	Muterspaugh et al. (2010)
8	21145+1000	STT 535AB	104858	2018.6523	0.0	0.0	−0.1	0.0	Muterspaugh et al. (2008)
9	13100+1732	STF 1728AB	64241	2019.0599	0.0	−0.1	0.0	0.0	Muterspaugh et al. (2015)
10	21145+1000	STT 535AB	104858	2019.6927	0.0	+0.1	0.0	+0.1	Muterspaugh et al. (2008)
10	22409+1433	HO 296AB	111974	2019.6955	+0.1	+0.1	−0.1	−0.5	Muterspaugh et al. (2010)

(This table is available in machine-readable form.)

Table 3
Binary Star Speckle Measures

WDS (α,δ J2000.0)	HR, ADS DM, etc.	Discoverer Designation	HIP	JY (2000+)	θ (°)	ρ ($''$)	Δm (mag)	λ_c (nm)	$\Delta\lambda$ (nm)
00126+4419	HD 802	LSC 5	1011	19.0488	314.0	0.5792	<4.64	562	44[a]
				19.0488	313.7	0.5821	4.90	832	40
00174+1852	BD+18 24	HDS 39	1389	17.7953	247.4	1.5883	<2.54	692	40[a]
				17.7953	247.5	1.5897	<1.69	880	50[a]
00182+5225	HD 1384	YSC 79	1460	19.0488	333.2	0.3112	3.45	562	44
				19.0488	333.4	0.3140	3.38	832	40

Notes.
[a] The magnitude difference appears as an upper limit because the observation may be affected by the speckle decorrelation effect discussed in the text.
[b] Quadrant determination inconsistent with other published measures.
[c] Quadrant determination possibly inconsistent with other published measures.

(This table is available in its entirety in machine-readable form.)

arcseconds; (8) the magnitude difference (Δm) of the pair in the filter used; (9) the center wavelength of the filter (λ_c); and (10) the FWHM of the filter transmission ($\Delta\lambda$). Note that although observation epochs were stated in Besselian years in our previous papers in this series, here we have used Julian years to align with IAU recommendations. If the Besselian date is needed, it can be obtained by using

$$\mathrm{BY} = (\mathrm{JY} - 0.041439661) \cdot 1.000021359. \quad (1)$$

Thirty-one pairs in the table have no previous detection of the companion in the Fourth Catalog of Interferometric Measures of Binary Stars (Hartkopf et al. 2001b),[14] and we therefore propose discoverer designations of LSC (Lowell-Southern Connecticut) 131–161 here. (This continues the collection of LSC discoveries detailed in Paper IX of this series.) All of these objects have been confirmed as a binary in at least one other observation not appearing here; a future paper will present the relative astrometry and photometry for those confirming observations.

Figure 1 visually summarizes the aggregate results from Table 3 in two ways. In Figure 1(a), we plot the magnitude difference obtained as a function of the log of the separation. A curve that illustrates our basic detection capability as determined in Paper IX (Horch et al. 2020) is plotted with the data; this has two quasi-linear portions of different slopes and assumes a detection limit of $\Delta m = 0$ at the diffraction limit. The curve increases steeply from the diffraction limit, but a "knee" is seen at approximately $0\farcs1$. For separations above this, the slope flattens out and is more modest throughout the remainder of the separation axis, until detection is no longer possible due to the field-of-view restrictions on the speckle cameras we used. We see in the figure that the current data set fills the presumed discovery space of DSSI subject to the conservative assumption that the detection limit curve must go

[14] http://astro.gsu.edu/wds/int4.html

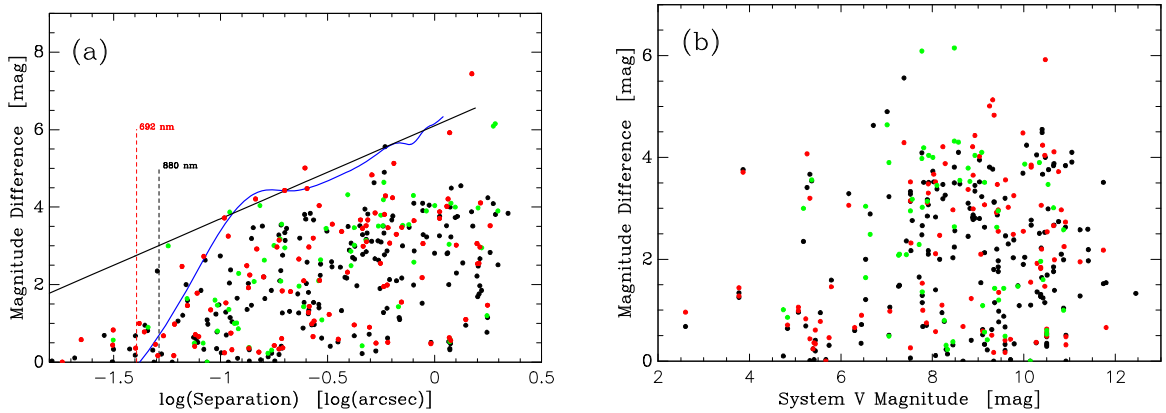

Figure 1. (a) Magnitude difference as a function of separation for the observations in Table 3. (b) Magnitude difference as a function of system V magnitude. In both panels, the color of the plot symbol indicates the filter wavelength used for the observation: green is 562 nm, red is 692 nm, and black is either 832 nm (for NESSI observations) or 880 nm (for DSSI observations). In (a), the blue curve indicates a detection limit curve for LDT observations, and the black line is drawn such that it matches the blue curve above a separation of $0\farcs1$.

to a magnitude difference of zero at the diffraction limit. In addition, some results appear at smaller separations than the diffraction limit with magnitude differences higher than the curve shown. We have argued in past papers that, when systems are known to be binary through other observations, the fits we obtain below the diffraction limit yield reasonable results, albeit with some decrease in precision, as in e.g., Horch et al. (2020). The small-separation points above the blue detection limit curve drawn fit into that category. The black line in the diagram continues the more modest slope to smaller separations, and the data indicate that this may be a truer estimate of the sensitivity than the steeper slope, at least down to separations as small as the diffraction limit. In Figure 1(b), the magnitude difference obtained is shown as a function of the system V magnitude; we see here that virtually all systems reported here are brighter than 12th magnitude. In these data, we do not detect a dependence on the dynamic range sensitivity for $V = 5$–12.

4. Analysis of the Data

4.1. Astrometric Precision

In order to characterize the astrometric precision of the measures in Table 3, we first utilize the fact that, because DSSI and NESSI take simultaneous observations in two filters, most of the measures listed in Table 3 are paired. Thus, we examine the differences between the separation (ρ) and the position angle (θ) obtained between the two filters for the same epoch of observation. These are shown in Figure 2 for both coordinates of the relative position. For separation, there is no obvious trend in either the differences or in their scatter as a function of average separation. These measures have an average difference of 0.40 ± 0.22 mas, and their standard deviation is 2.93 ± 0.16 mas. The former perhaps indicates a slight systematic difference between the scale values obtained in the two channels of the instrument. In contrast, the scatter in the difference in position angle increases as the separation decreases; this indicates that at smaller separations, the same positional uncertainty subtends a larger angle. The average value here is $-0\fdg08 \pm 0\fdg11$, indicating no measurable offset between the two channels of the instrument. If we assume that the positional uncertainty is the same in the orthogonal direction to the separation compared with the direction of separation itself, we would expect the scatter in the position angle differences to vary as

$$\delta\theta = \arctan\left(\frac{\delta\rho}{\rho}\right) = \arctan\left(\frac{2.93\ \text{mas}}{\rho}\right), \tag{2}$$

where $\delta\theta$ is the uncertainty in the position angle difference and $\delta\rho$ is the uncertainty in the separation difference. We have drawn this curve in Figure 2(b), and it appears to be consistent with the scatter in the data. In Figure 2, we also plot the separation and position angle differences as a function of the average of the magnitude difference obtained in the two channels of the instrument. These show a slight trend toward larger values as the magnitude difference increases, which is not unreasonable when the signal-to-noise ratio of the secondary star decreases. Because the data in all of the plots in Figure 2 are differences of two measures that presumably have similar uncertainties, we can infer that the uncertainty of a given single measure in Table 3 is reduced from the above standard deviation by a factor of $\sqrt{2}$, to 2.07 ± 0.11 mas, and the position angle uncertainty is similarly reduced.

We also studied cases in Table 3 where an orbit determination exists in the literature and we compare our measures with the ephemeris positions derived from the published orbital elements. We confine ourselves to objects with orbits in the Sixth Orbit Catalog (Hartkopf et al. 2001a)[15] of Grade 2 or better and which have uncertainties in the published orbital elements available in the Sixth Orbit Catalog. We further restrict ourselves to those objects that have observations in two filters at the same epoch in Table 3. Figure 3 shows the residuals obtained, where we have averaged the position angle and separation between the channels for each pair of observations and plot that as a single point in Figure 3. We have also drawn the same curves as in Figures 2(a) and (b), although because we have averaged two independent measures to obtain each data point here, we also divided the internal precision number by $\sqrt{2}$, which is how the resulting uncertainty would decrease for two truly independent samples of the same uncertainty. Thus, the lines drawn in Figure 2 for separation were at ± 2.07 mas, here they are drawn at $\pm 2.07/\sqrt{2} = \pm 1.46$ mas, and the curves drawn for the position angle are likewise modified.

[15] http://astro.gsu.edu/wds/orb6.html

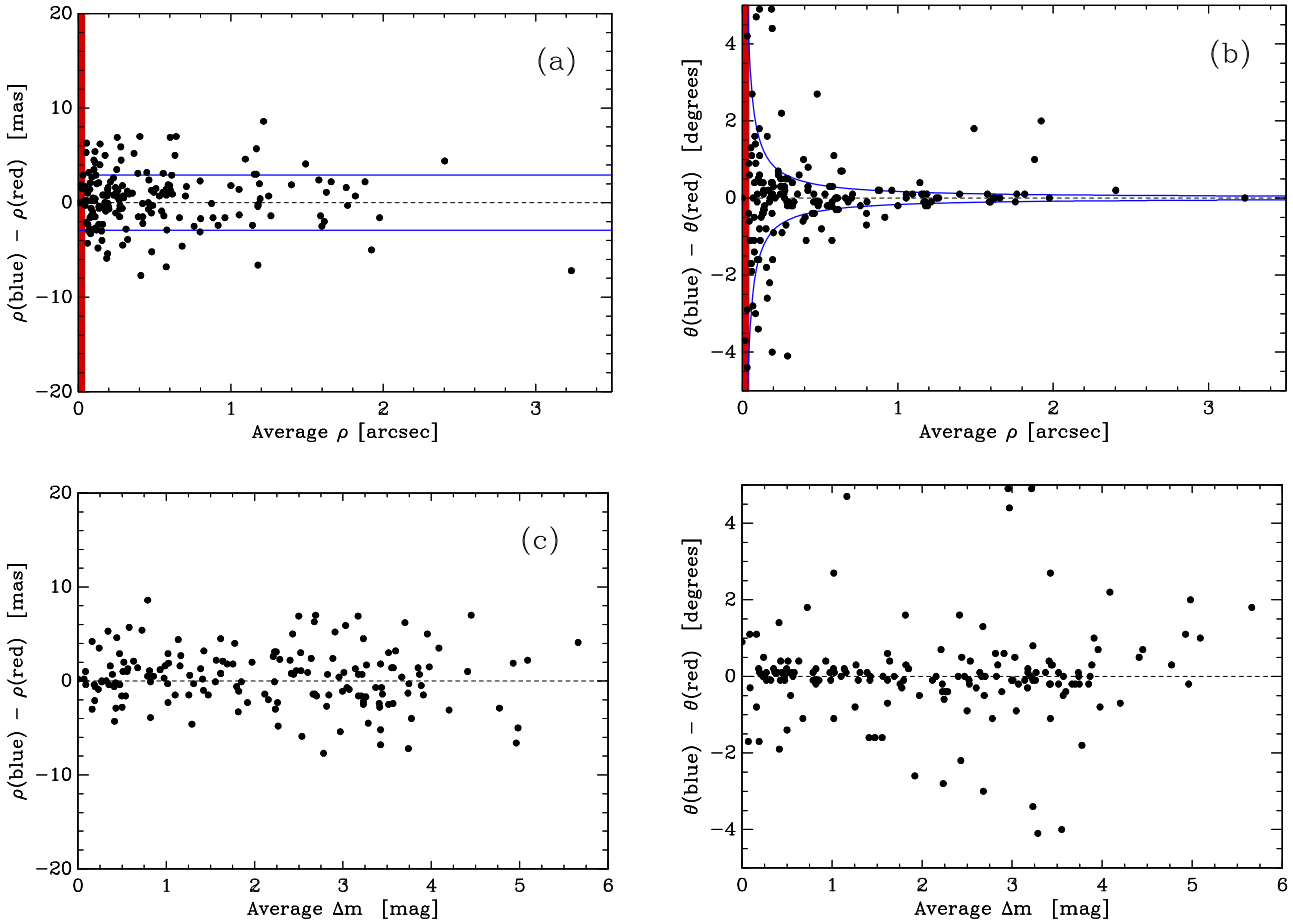

Figure 2. Differences in the astrometric results obtained between paired observations at the same epoch. (a) Differences in separation as a function of average separation. (b) Differences in position angle as a function of average separation. In both plots, a dashed line at a difference of zero is drawn to guide the eye, and the blue curves indicate the $\pm 1\sigma$ in estimated internal repeatability of individual measures as a function of separation as discussed in the text. For differences in separation, that is simply the standard deviation of the measures, and for position angle, it is proportional to arctan $\delta\rho/\rho$. In both (a) and (b), the red bar at the left marks the region below the formal diffraction limit. (c) Differences in separation as a function of magnitude difference. (d) Differences in position angle as a function of magnitude difference. In these latter two panels, a dashed line at zero is again drawn to guide the eye.

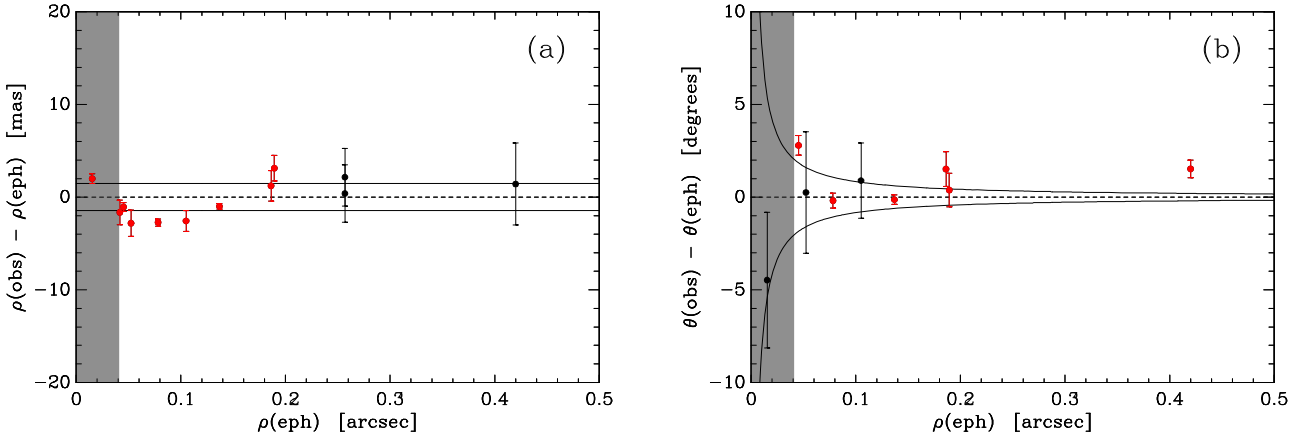

Figure 3. Residuals obtained when comparing with ephemeris position for objects in Table 3 that have a Grade 1 or Grade 2 orbit in the Sixth Orbit Catalog. The error bars drawn are those of the ephemeris prediction, based on the published uncertainties in the orbital elements. (a) Separation residuals as a function of average separation. The red points are objects with ephemeris uncertainties of less than 2 mas. (b) Position angle residuals as a function of average separation. Here, the red points indicate position angle uncertainties of less than 1°. In both plots, the expected 1σ uncertainty from our internal precision study is drawn as discussed in the text, and the gray regions at the left of each plot mark separations below the formal diffraction limit of the LDT at 692 nm.

The results indicate complete consistency with the internal repeatability study. For separation, the average is -0.13 ± 0.61 mas with a standard deviation of 2.10 ± 0.43 mas. In position angle, we find an average residual of $0\overset{\circ}{.}06 \pm 0\overset{\circ}{.}51$ and a standard deviation of $1\overset{\circ}{.}78 \pm 0\overset{\circ}{.}36$. We conclude that there are no identifiable sources of systematic error in the data set and that our individual measures in Table 3 have an average uncertainty of 2.07 mas in separation and arctan(2.07 mas$/\rho$) in position angle.

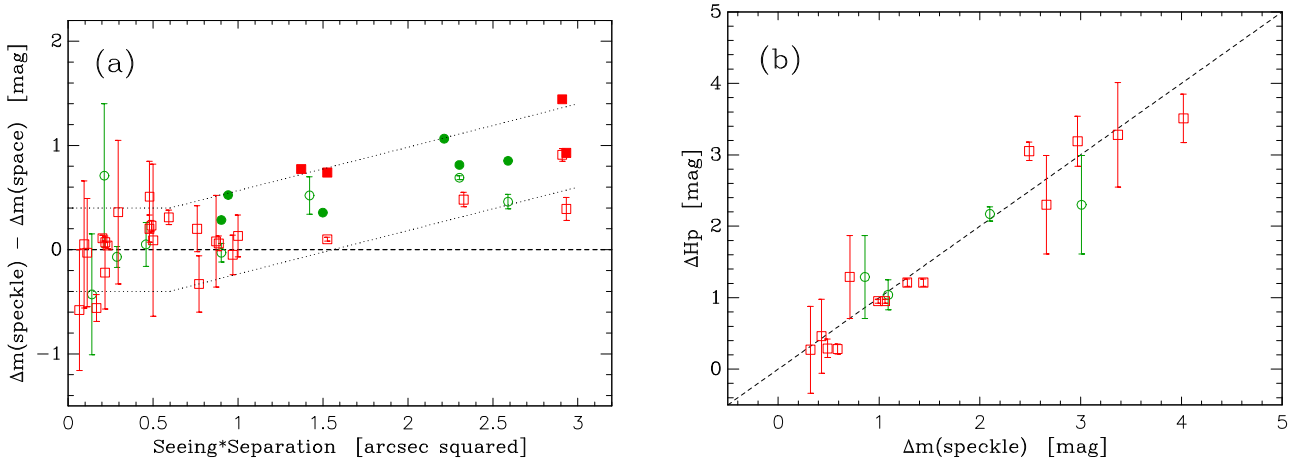

Figure 4. A comparison of speckle magnitude difference vs. the Gaia or Hipparcos magnitude difference. (a) The difference between these two measures as a function of seeing times separation of the speckle observation. (b) For those objects with seeing times separation below 0.6 arcsec^2, the space-based magnitude difference is plotted as a function of the speckle magnitude difference. In both plots, red square symbols indicate that the speckle magnitude difference is in the 692 nm filter, and green circles indicate that the speckle magnitude difference is in the 562 nm filter. The symbols are drawn as filled in either case if the uncertainty in the space-based measure is less than 0.1 mag.

4.2. Photometric Precision

Regarding the photometric precision of our measures, we have compared our results to space-based measures in two ways. First, as in previous papers in this series, we use data in the Hipparcos Catalog, although the H_p filter is not a good match for any of the filters we use in speckle imaging as it is wider and bluer than any of the filters we have used in our observations. In addition, a number of the stars in Table 3 do not have component information in the Hipparcos Catalog. On the other hand, high-precision data are available from Gaia in the G and R_p filters, which are reasonably similar to our 562 and 692 nm filters, respectively. However, for separations below 1″, which is the vast majority of our sample, there is almost nothing available in EDR3. Both samples are further complicated by the presence of triples, which we resolve in our observations but are not resolved in the Gaia or Hipparcos results. Examples in this category are not used for a comparison. We also removed one other object, HIP 63942, because the uncertainty in the flux in the Gaia R_p filter was very large in EDR3, and we do not consider systems with Δm less than 0.25, as the speckle magnitude differences typically have larger scatter and uncertainties about quadrant determinations in that range. Setting all of these objects aside, we are left with a relatively small sample of only 33 observations to study in detail.

Nonetheless, we show a comparison between the space-based and speckle results in Figure 4. In panel (a), we plot the difference between the speckle Δm and the space-based value as a function of seeing times separation of the speckle observation. In previous papers, we have used this quantity as a way to judge the isoplanicity of the observations and thus the reliability of the photometry. The larger this quantity is, then the less the speckle patterns between the primary and secondary stars will resemble each other, so that in the standard analysis, a secondary will appear fainter than it actually is. Therefore, the difference between the speckle Δm and that obtained from a space-based source should be near zero for small values of seeing times separation and grow as this quantity gets larger. This is indeed the general trend in Figure 4(a).

As in our previous papers, if we confine our attention to those observations in Table 3 that have seeing times separation less than 0.6 arcsec^2, then these should be relatively unaffected by non-isoplanicity, and therefore correlate well with the space-based values. This is shown in Figure 4(b). It may be seen here that all of the objects in this subsample are Hipparcos stars, and some have sizable uncertainties. However, within the uncertainty, the correlation is quite good. The average uncertainty $\delta(\Delta H_p)$ for the points in Figure 4(b) is 0.327 mag; if we subtract this value in quadrature from the standard deviation of the plot residuals, an estimate of the typical uncertainty in the speckle Δm can be made; this results in a value of 0.092 mag, which is comparable to what we have quoted in earlier papers in this series (typically 0.1–0.15 mag). We conclude that, though this result is not as statistically robust as in the larger samples studied in previous papers, it remains consistent with them in terms of the photometric precision of the measures we present. Although we did not compare our results at 832 and 880 nm directly with the space-based measures, there are two cases in Table 3 where we report three individual measures at these wavelengths (HIP 55605 and HIP 57058). In these cases, the average standard deviation in the Δm is 0.13 ± 0.09, indicating that at least the internal precision appears comparable to the other wavelengths, to the extent that we can determine.

5. Orbit Calculations

A set of 25 systems in Table 3 have shown significant relative motion since they were discovered, and the new data, together with previous measures in the literature, permit the calculation of first orbital elements in some cases. We use the orbit code described in MacKnight & Horch (2004) for this purpose, which performs a grid search based on a low and high value of each orbital element provided, and then after determining the best fit to the data on the grid, it performs a downhill simplex calculation to reach the global minimum in reduced-χ^2. To estimate uncertainties in the final orbital elements, we perform the orbit calculation many times, typically 50–100 times, and in each case we throw in normally distributed offsets to the position angle and separation values used in the calculation. The standard deviations of these offsets

Table 4
Visual Orbital Elements for 25 Systems

WDS	Discoverer Designation	HIP	Spectral Type[a]	P (yr)	a ($''$)	i (°)	Ω (°)	T_0 (JY)	e	ω (°)
00132+2023	HDS 29	1055	K7V	78.8	0.4233	136.4	331.7	2062.4	0.895	348.3
				2.3	0.0067	7.6	3.1	2.1	0.021	4.0
02164+0438	YR 8	10596	F0V	48.9	0.1080	101.7	332.94	2055.	0.324	82.
				6.7	0.0095	1.9	0.89	21.	0.077	24.
02167+0632	YSC 20	10616	K0	13.61	0.1255	22.9	192.	2010.705	0.4529	248.
				0.14	0.0017	4.0	12.	0.032	0.0078	12.
03376+2121	PAT 1	16908	K0V	110.0	0.8475	111.61	292.0	2071.06	0.434	251.66
				1.4	0.0081	0.32	1.1	0.60	0.016	0.71
04268+1240	WOR 15	20745	K2	40.9	0.314	144.	136.	2037.1	0.811	319.
				3.3	0.047	14.	19.	3.3	0.024	16.
05009+6107	HDS 650	23317	K5	39.3	0.242	93.8	341.0	2058.3	0.49	196.
				4.7	0.025	1.5	2.0	8.6	0.16	27.
08289–1552	RST 4403	41609	K2V	205.6	1.191	160.0	67.5	2149.6	0.183	25.8
				2.4	0.021	5.9	2.2	3.8	0.034	2.8
08447–2126	HDS 1260A-BC	42910	K7V	106.1	0.764	149.	248.7	2126.4	0.167	97.
				5.3	0.027	10.	8.8	3.1	0.066	13.
08447–2126	TOK 395BC	42910	M3V?	9.06	0.1158	105.9	7.7	2008.2	0.551	350.
				0.58	0.0045	2.7	2.9	2.5	0.080	11.
10320+0831	YSC 39	51571	K5V	178.9	1.083	129.5	50.95	2000.07	0.274	331.4
				5.4	0.015	1.6	0.79	0.60	0.012	2.0
11114+4150	HDS 1593	54663	K2	36.8	0.265	70.9	329.0	2000.2	0.269	74.6
				3.0	0.013	3.2	1.5	1.1	0.040	5.8
11235+0701	BAG 24Aa,Ab	55605	K4V	20.80	0.227	160.	316.	2014.29	0.290	386.
				0.11	0.010	12.	19.	0.57	0.030	22.
11418+0508	LSC 141	57058	K4V	3.728	0.0807	32.6	110.2	2017.949	0.338	269.4
				0.057	0.0016	2.2	9.4	0.020	0.019	9.6
11471–1149	RST 3756	57494	K4.5V	128.0	1.164	132.15	151.6	2044.1	0.108	89.7
				2.7	0.010	0.96	2.0	1.5	0.027	5.5
11539+1402	YSC 96	58006	F0	36.8	0.123	36.0	86.	2006.5	0.13	94.
				4.9	0.014	6.8	13.	9.9	0.13	25.
13331+4316	COU 1754	66110	K8V	125.5	0.6524	94.865	171.25	2056.4	0.189	230.13
				2.0	0.0059	0.073	0.34	1.2	0.018	0.21
13450+0206	HDS 1935	67086	K5	209.	0.730	146.7	7.7	2188.	0.270	209.
				18.	0.036	4.0	9.7	21.	0.064	11.
14136+5522	HDS 1995	69488	K0	40.9	0.333	127.3	241.6	2028.9	0.387	248.2
				1.7	0.013	1.8	4.2	1.6	0.047	3.1
14330+0656	YSC 6	71142	K0	57.6	0.199	40.5	246.2	2044.	0.122	33.
				9.0	0.025	6.0	3.8	12.	0.059	29.
14136+5522	HDS 2211	76768	K5V	79.5	0.592	136.6	272.8	2042.6	0.679	49.3
				2.3	0.015	3.2	3.5	1.1	0.023	4.0
17577–2143	HDS 2530	87925	K6+V	54.9	0.5214	63.8	148.2	1999.5	0.585	249.82
				1.6	0.0073	1.5	1.4	0.5	0.013	0.75
19153+2454	HDS 2724	94622	K5	8.450	0.152	116.4	284.9	2005.2	0.329	212.
				0.025	0.015	3.9	6.7	1.1	0.068	40.
19233–0635	HDS 2745	95299	K3/4(V)	161.7	0.893	145.9	18.1	2124.63	0.549	209.7
				1.0	0.016	3.6	1.0	0.59	0.031	1.8
19467+4421	YSC 136	97321	F9IV-V	4.813	0.0831	64.3	89.9	2010.524	0.180	261.0
				0.019	0.0022	1.3	1.7	0.047	0.022	3.7
23464–2302	TOK 375	117247	K2+V	12.5	0.1426	165.4	232.2	2022.47	0.429	149.2
				1.0	0.0037	5.9	8.0	0.78	0.044	9.0

Notes.
[a] From SIMBAD (Wenger et al. 2000).

(This table is available in machine-readable form.)

are 2.5 mas in separation and $0.0025/\rho$ degrees in position angle. Of course, the uncertainties obtained should still be viewed as formal and not necessarily representing the true uncertainty of each orbital element; most of the orbits presented are fits to only a portion of the orbital path or represent sparse coverage of the orbital ellipse. Further observations will be needed to refine these orbits, and we highlight them here in an attempt to encourage other observers to take more data on these systems in the coming years.

The visual orbital elements obtained are shown in Table 4, where the orbits span a range in periods of 3–206 yr and semimajor axes of $0''.08$–$1''.2$. All of these are cases for which the orbit has been calculated for the first time, and most stars have been previously identified as K dwarfs. The first column

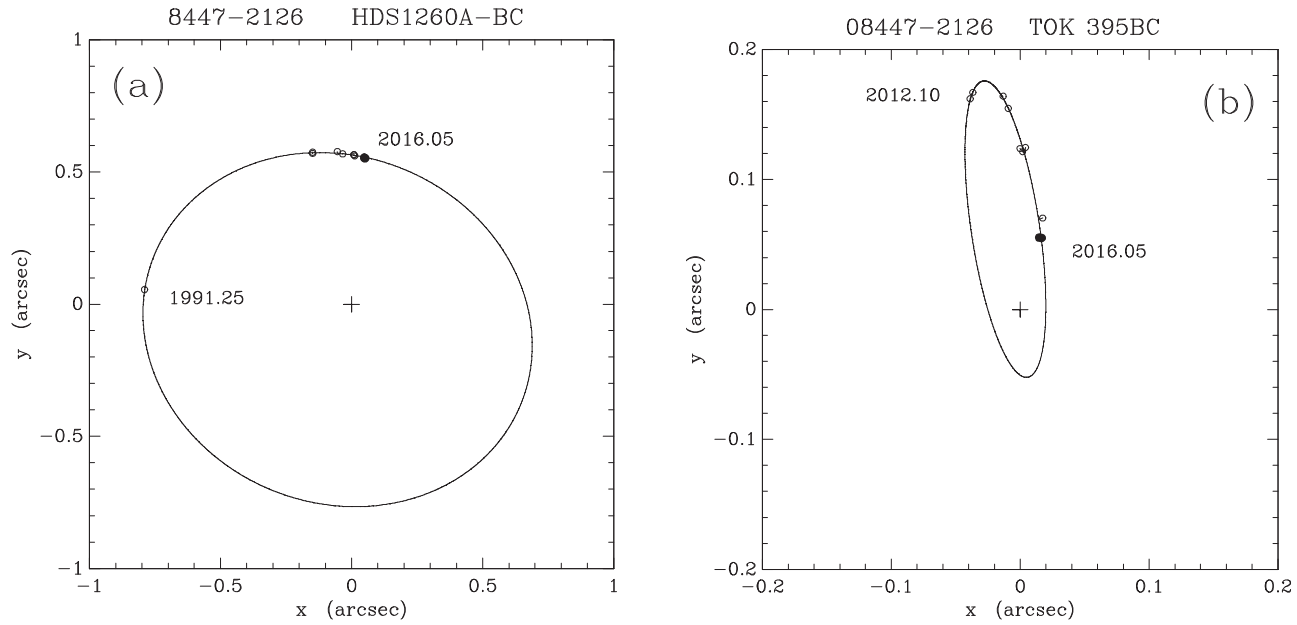

Figure 5. Visual representations of the orbits in Table 4 for the triple system HIP 42910. (a) HDS 1260A-BC; (b) TOK 395BC. In all plots, north is down and east is to the right. The cross marks the origin in each panel. Measures appearing in Table 3 are shown as filled circles while previous measures listed in the fourth Interferometric Catalog are drawn as open circles, and line segments are drawn from the ephemeris position on the orbit to each data point. The positions shown for the BC component in panel (a) are obtained by averaging the published positions of AB and AC for each epoch.

gives the discoverer designation from Table 3 followed by the spectral type as it appears in SIMBAD[16] (Wenger et al. 2000). Column 3 shows the Hipparcos number, and the remaining columns contain the seven standard visual orbital elements and their estimated uncertainties.

5.1. The Triple System HIP 42910

HIP 42910 was first discovered to be binary in observations taken with the Hipparcos satellite (ESA 1997), yet no speckle measures of the pair were taken until our work at the WIYN telescope in 2012 (Horch et al. 2017). That observation also revealed that the fainter component was a small-separation pair, but the work was published after observations of Tokovinin et al. (2015), thus the BC component bears the discoverer designation of those authors. Since 2012, a very nice sequence of speckle observations has been taken and published by both groups, including the most recent ones that are included in this paper in Table 3. The longer time baseline of the wider component (A–BC) allows for a reasonable orbit calculation there (with $P = 106.1$ yr), while the BC pair has a much shorter period and smaller separation, and therefore the current group of speckle measures for that pair already covers about one-third of the orbital ellipse ($P = 9.06$ yr). The orbits for both components are shown in Figure 5. SIMBAD lists the composite spectral type as K7V and observations by the RAVE project (Kordopatis et al. 2013) indicate a metallicity near solar ($[m/H] = 0.08 \pm 0.09$).

5.2. A Spectroscopic-visual Orbit for HD 173093=YSC 133

5.2.1. Spectroscopic Observations

Spectroscopic observations of HD 173093 (=HIP 91880 = YSC 133) at Kitt Peak National Observatory (KPNO) began a decade before it was learned that this system was also being observed with speckle interferometry. Discovery of our mutual interest and our complementary observing techniques led to the current effort to determine the orbital and physical properties of the system.

From 2001 June through 2014 July we obtained 33 spectroscopic observations of HD 173093 at KPNO with the 0.9 m coudé feed telescope and spectrograph. The initial 11 observations were acquired when the star was included in a solar-type star survey of Abt & Willmarth (2006). However, HD 173093 was dropped from that survey after the sample was limited to stars within 25 pc of the Sun. From those initial observations it was determined to be a double-lined binary and so additional observations were obtained, which revealed the star to be a triple system.

The KPNO spectra were acquired with various gratings and CCD detectors and so resulted in spectra that had different wavelength ranges and different resolutions. The various combinations are listed in Table 5. Additional information is provided in Abt & Willmarth (2006), Fekel et al. (2019), and Horch et al. (2020).

The KPNO CCD spectra were calibrated and extracted with standard IRAF tasks, after which radial velocities were measured with the IRAF task FXCOR (Fitzpatrick 1993). Template stars for the cross-correlations were from the list of Scarfe (2010) or Nidever et al. (2002). A comparison of velocities from these two sources shows agreement within 0.1 km s^{-1} (Horch et al. 2020). Between 2008 May and 2020 June we extensively supplemented the KPNO spectra with an additional 291 usable spectroscopic observations acquired at Fairborn Observatory in southeast Arizona. The spectra were obtained with the Tennessee State University 2 m Astronomical Spectroscopic Telescope (AST) and fiber-fed echelle spectrograph (Eaton & Williamson 2004). Our initial detector was a SITe ST-002A CCD with 15 μm pixels. In the summer of 2011 that CCD was replaced with a larger format Fairchild 486 CCD that also had 15 μm pixels (Fekel et al. 2013). Additional information is provided in

[16] https://simbad.u-strasbg.fr/simbad

Table 5
Telescopes and Instruments for Spectroscopic Observations[a]

Date yr m d	Helio. Julian Date −2,400,000	Telescope	Instrument, Grating, CCD	Resolution $\lambda/\Delta\lambda$ (2 pix.)
2001 6 13	52073	KPNO coudé feed	coudé spec.,A,F3KB	31,250
2001 6 14	52074	KPNO coudé feed	coudé spec.,A,F3KB	31,250
2001 6 15	52075	KPNO coudé feed	coudé spec.,A,F3KB	31,250
2001 6 16	52076	KPNO coudé feed	coudé spec.,A,F3KB	31,250
2002 5 8	52402	KPNO coudé feed	coudé spec.,A,F3KB	31,250
2002 5 9	52403	KPNO coudé feed	coudé spec.,A,F3KB	31,250
2002 9 28	52545	KPNO coudé feed	coudé spec.,A,F3KB	31,250
2002 9 30	52547	KPNO coudé feed	coudé spec.,A,F3KB	31,250
2002 10 9	52556	KPNO coudé feed	coudé spec.,A,F3KB	31,250
2002 10 10	52557	KPNO coudé feed	coudé spec.,A,F3KB	31,250
2002 10 11	52558	KPNO coudé feed	coudé spec.,A,F3KB	31,250
2003 3 11	52710	KPNO coudé feed	coudé spec.,A,TI5	30,000
2004 6 16	53172	KPNO coudé feed	coudé spec.,A,TI5	30,000
2004 6 17	53173	KPNO coudé feed	coudé spec.,A,TI5	30,000
2005 6 11	53532	KPNO coudé feed	coudé spec.,A,TI5	30,000
2005 6 13	53534	KPNO coudé feed	coudé spec.,A,TI5	30,000
2005 6 14	53535	KPNO coudé feed	coudé spec.,A,TI5	30,000
2006 9 23	54001	KPNO coudé feed	coudé spec.,A,TI5	30,000
2006 9 28	54006	KPNO coudé feed	coudé spec.,A,TI5	30,000
2007 9 26	54369	KPNO coudé feed	coudé spec.,A,TI5	30,000
2007 11 4	54408	KPNO coudé feed	coudé spec.,A,TI5	30,000
2008 4 27	54583	KPNO coudé feed	coudé spec.,A,TI5	30,000
2008 5 7[b]	54593	TSU AST 2 m	spec.,echelle,SITe ST-002A	35,000
2009 4 29	54950	KPNO coudé feed	coudé spec.,A,TI5	30,000
2009 4 30	54951	KPNO coudé feed	coudé spec.,A,TI5	30,000
2009 6 20	55002	KPNO coudé feed	coudé spec.,A,TI5	30,000
2009 6 21	55003	KPNO coudé feed	coudé spec.,A,TI5	30,000
2010 4 27	55313	KPNO coudé feed	coudé spec.,A,TI5	30,000
2011 10 12[c]	55846	TSU AST 2 m	spec.,echelle,Fairchild 486	25,000
2012 10 9	56209	KPNO coudé feed	coudé spec.,echelle,T2KB	72,000
2013 4 20	56402	KPNO coudé feed	coudé spec.,A,STA3	26,600
2013 5 22	56434	KPNO coudé feed	coudé spec.,A,STA3	26,600
2013 10 26	56591	KPNO coudé feed	coudé spec.,echelle,T2KB	72,000
2014 4 24	56771	KPNO coudé feed	coudé spec.,echelle,T2KB	72,000
2014 7 30	56868	KPNO coudé feed	coudé spec.,echelle,T2KB	72,000

Notes.
[a] See Table 6 for a complete list of observing dates, RVs, and sources.
[b] First of 158 observations.
[c] First of 133 observations.

Table 5. Eaton & Williamson (2007) discussed the reduction and wavelength calibration of the raw spectra.

Fekel et al. (2009) provided a general description of the velocity measurement procedure. In particular for HD 173093, we used a solar line list that consists of 168 mostly neutral metallic lines in the spectral region 4920–7100 Å and fitted each line with a rotational broadening function (Fekel & Griffin 2011; Lacy & Fekel 2011).

All of our spectroscopic observations and velocities for HD 173093 (324 in total) are listed in Table 6. These show that HD 173093 is a triple system with the lines of all three components visible in the spectrum. The lines of the components can be distinguished from each other because of their different relative line depths and somewhat different widths. However, velocity measurement of the lines is more difficult than usual because the semiamplitudes of the stars in the short-period system are not large enough to completely separate the three sets of lines at the resolutions of our various spectra. Therefore, in both the KPNO and AST spectra, the lines of at least two of the three components, the long-period component and one of the short-period components, are always at minimum partly blended. Thus, the measurement of the blended lines consisted of simultaneous fits to the blended components. Our unpublished velocities for several IAU solar-type velocity standards show that our velocities with the SITe CCD have a $-0.3\,\mathrm{km\,s^{-1}}$ shift relative to the results of Scarfe (2010), and for the Fairchild CCD there is a $-0.6\,\mathrm{km\,s^{-1}}$ shift. Thus, depending on the detector used, we have added $0.3\,\mathrm{km\,s^{-1}}$ or $0.6\,\mathrm{km\,s^{-1}}$ to the measured AST velocities.

Our radial velocities from the two observatories are tied to the IAU standards observed by Scarfe (2010). Thus, there is no significant zero-point shift in the velocities from the two observatories (Willmarth et al. 2016).

5.2.2. Combined Orbit

Using both the spectroscopic data and speckle observations of HD 173093, we were able to calculate a combined visual-spectroscopic orbit of this triple system using the methods outlined in Muterspaugh et al. (2010). Fitted velocities obtained from the

Table 6
Radial Velocity Data

Modified Julian Date	Measured RV, Aa (km s^{-1})	Model RV, Aa (km s^{-1})	$O-C$,Aa (km s^{-1})	σ_{Aa} (km s^{-1})	Measured RV, Ab (km s^{-1})	Model RV, Ab (km s^{-1})	$O-C$,Ab (km s^{-1})	σ_{Ab} (km s^{-1})	Measured RV, B (km s^{-1})	Model RV, B (km s^{-1})	$O-C$,B (km s^{-1})	σ_{B} (km s^{-1})	Set[a]
52073.4155	⋯	⋯	⋯	⋯	−71.000	−71.160	0.160	0.880	⋯	⋯	⋯	⋯	1[b]
52074.4101	⋯	⋯	⋯	⋯	⋯	⋯	⋯	⋯	−41.700	−42.153	0.453	0.580	1
52075.3773	⋯	⋯	⋯	⋯	−52.100	−50.012	−2.088	0.880	−41.100	−42.134	1.034	0.580	1
52402.4801	−76.700	−77.418	0.718	0.960	−34.700	−34.878	0.178	0.880	−34.700	−34.318	−0.382	0.580	1
52403.4793	⋯	⋯	⋯	⋯	−72.300	−73.018	0.718	0.880	⋯	⋯	⋯	⋯	1
52545.1551	⋯	⋯	⋯	⋯	−81.200	−81.186	−0.014	0.880	⋯	⋯	⋯	⋯	1
52547.1323	⋯	⋯	⋯	⋯	⋯	⋯	⋯	⋯	−28.900	−29.586	0.686	0.580	1
52556.0851	−76.800	−77.039	0.239	0.960	⋯	⋯	⋯	⋯	⋯	⋯	⋯	⋯	1
52557.0857	⋯	⋯	⋯	⋯	−81.100	−81.894	0.794	0.880	⋯	⋯	⋯	⋯	1
52558.0997	−79.100	−79.875	0.775	0.960	⋯	⋯	⋯	⋯	⋯	⋯	⋯	⋯	1
52709.533	−71.900	−70.542	−1.358	1.004	−49.700	−50.028	0.328	0.679	−24.600	−25.340	0.740	1.518	2
53172.3861	−20.200	−19.705	−0.495	0.710	−63.200	−62.948	−0.252	0.679	−65.300	−65.322	0.022	1.518	2
53173.3669	−55.200	−56.348	1.148	1.004	−24.400	−24.302	−0.098	0.679	−64.300	−65.310	1.010	1.518	2
53532.4292	−56.100	−56.438	0.338	1.004	−29.600	−29.808	0.208	0.679	−60.700	−59.809	−0.891	1.518	2
53534.4298	−66.800	−65.146	−1.654	1.004	−20.800	−20.652	−0.148	0.679	−61.400	−59.778	−1.622	1.518	2
53535.4437	−25.400	−24.126	−1.274	1.004	−64.500	−63.944	−0.556	0.679	−62.400	−59.763	−2.637	1.518	2
54001.1377	−66.400	−65.699	−0.701	1.004	−27.700	−26.927	−0.773	0.679	−55.700	−53.043	−2.657	1.518	2
54006.1433	−66.800	−67.805	1.005	1.004	−24.800	−24.777	−0.023	0.679	−51.500	−52.972	1.472	1.518	2
54369.1752	−71.200	−71.135	−0.065	1.004	−27.900	−26.634	−1.266	0.679	−49.300	−47.699	−1.601	1.518	2
54408.0740	−29.100	−28.136	−0.964	1.004	−73.000	−72.611	−0.389	0.679	−49.200	−47.096	−2.104	1.518	2
54583.4562	−66.600	−66.203	−0.397	1.004	−34.900	−35.393	0.493	0.679	−45.700	−44.207	−1.493	1.518	2
54593.4369	−68.700	−68.588	−0.112	0.370	−33.600	−33.320	−0.280	0.735	−43.500	−44.162	0.662	0.520	3

Notes.
[a] Set 1 = KPNO velocities obtained by D. Willmarth, Set 2 = KPNO velocities obtained by F. Fekel, Set 3 = Fairborn Observatory.
[b] In this and in the following lines of the Set 1 data, three dots indicate that the velocity for a given component was not used in the fit due to extensive line blending.

(This table is available in its entirety in machine-readable form.)

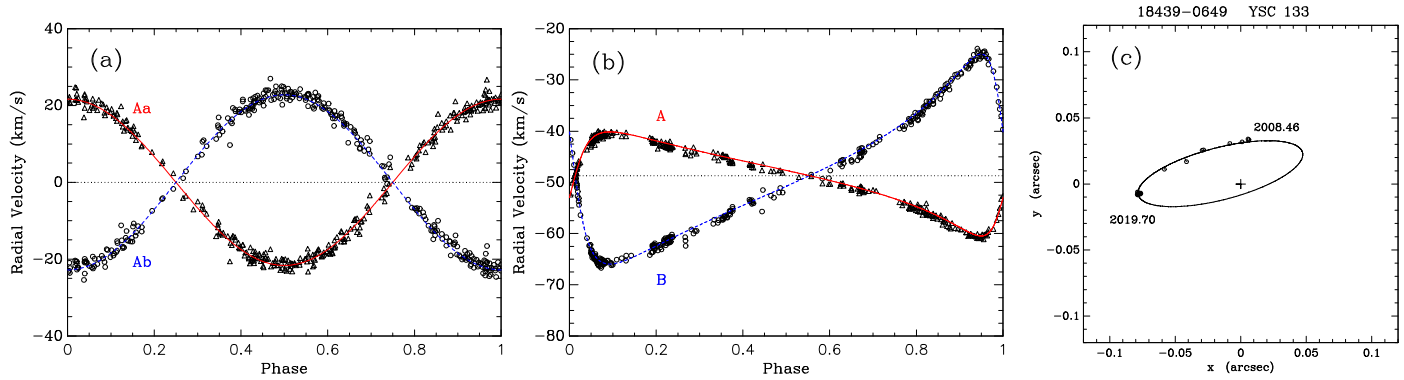

Figure 6. (a) Radial velocity curves for HD 173093Aa and Ab, with the motion due to the third component subtracted. (b) Radial velocity curves of HD 173093 A and B. (c) The visual orbit of YSC 133 = HD 173093AB as deduced from the combined astrometric and spectroscopic data set. Here, open circles represent previous measures in the literature and appearing in the Fourth Interferometric Catalog, filled circles are data points appearing in Table 3, and line segments are drawn from the ephemeris position on the orbit to each data point. The cross in the center marks the origin. North is down and east is to the right.

Table 7
Orbital Elements of HD 173093 = YSC 133

Parameter	Outer Orbit	Inner Orbit
P (days)	2642.5 ± 1.5	2.3580103 ± 0.0000014
T (MJD)	55470.03 ± 0.63	55999.72733 ± 0.00063
e	0.6109 ± 0.0013	0 (fixed)
a (mas)	80.09 ± 0.99	⋯
i (deg)	104.55 ± 0.27	11.308 ± 0.032 (or 168.692 ± 0.032)
Ω (deg)	286.62 ± 0.66	⋯
ω_A (deg)	254.98 ± 0.17	0 (assigned)
$\mathcal{M}_A$ ($M_\odot$)	2.857 ± 0.021	⋯
$\mathcal{M}_{Aa}$ ($M_\odot$)	⋯	1.467 ± 0.011
$\mathcal{M}_{Ab}$ ($M_\odot$)	⋯	1.390 ± 0.011
$\mathcal{M}_B$ ($M_\odot$)	1.416 ± 0.011	⋯
Distance (pc)	75.79 ± 0.71	⋯

model and observed minus calculated ($O - C$) residuals for each component are also shown in Table 6. The inner subsystem has a period of only 2.36 days, so it is inaccessible to our speckle observations. Because the inner orbit is so short, we tried the calculations two ways, first by fixing the eccentricity of the inner orbit to zero and next by allowing it to float. In either case, the elements of the outer orbit are unaffected, as are the derived masses of the three components and the distance to the system. For the purposes of the discussion in the next section, we will work with the numbers obtained from the zero-eccentricity case. (The eccentricity obtained in the second orbit was small but nonzero, 0.0056 ± 0.0014.) Radial velocity plots for both orbits and the visual orbit of the wider component are shown in Figure 6, and the orbital elements, masses, and the distance derived are shown in Table 7. The distance we determine (75.79 ± 0.71 pc) is slightly larger than the value implied by the Gaia EDR3 parallax (72.56 ± 0.38 pc) while the Hipparcos revised value (van Leeuwen 2007) straddles both (73.9 ± 2.3 pc), although with lower precision. However, the basic astrometric information on the Gaia DR3 sources, obtained by treating all of them as single stars, has already been provided in EDR3 and will not change for DR3 (Lindegren et al. 2021). As HD 173093 is unresolved in EDR3, this may be the source of the discrepancy.

Based on our results, HD 173093 is a hierarchical triple system with a long-period to short-period ratio of 1121. The inclinations of its two orbits (Table 7) are very different, 104°.6 for the outer orbit and 11°.3 for the inner orbit, so the orbits are clearly not coplanar. With such a large inclination difference, the eccentricity and inclination of the inner orbit can undergo periodic changes that are known as Kozai–Lidov cycles (Kozai 1962; Lidov 1962). According to theoretical analyses, the evolution of such triples is driven by the Kozai–Lidov modulation plus tidal friction. These processes produce an inner binary with a period of just a few days (Mazeh & Shaham 1979; Eggleton & Kiseleva-Eggleton 2001; Fabrycky & Tremaine 2007). In particular, Fabrycky & Tremaine (2007) predicted that the combination of Kozai–Lidov cycles and tidal friction typically results in inner binaries with periods less than 10 days. Their final short-period distribution had its peak at 3 days. Observationally, Tokovinin et al. (2006) surveyed 165 solar-type binaries and found that 96% of those with periods less than 3 days were triple. HD 173093, which has an inner orbit with a period of 2.36 days, is consistent with the results of Fabrycky & Tremaine (2007) and Tokovinin et al. (2006).

5.3. Individual Masses for Six Stars

The above orbital results afford us the opportunity to determine the individual masses of stars in the two triple systems discussed, HDS 1260 and HD 173093. Four of these masses are determined dynamically, whereas two rely on an assumption that those stars have the same mass. In preparation for a comparison between the masses and absolute magnitudes of these stars with the empirical data available in the most recent papers, we have used the data tables in Torres et al. (2010) for F,G,K stars together with the polynomial fit derived in Benedict et al. (2016). Specifically, we derive the following polynomial fit based on the previous reference for $1 \leqslant M_V < 9$:

$$\mathcal{M} = 2.371 - 0.2683 \cdot M_V - 0.0483 \cdot M_V^2 + 0.0131 \cdot M_V^3 - 0.000761 \cdot M_V^4, \quad (3)$$

where $\mathcal{M}$ represents the mass of the star. On the other hand, for $9 \leqslant M_V \leqslant 18$, and defining $x = M_V - 13.0$, Benedict et al. (2016) find that

$$\mathcal{M} = 0.19226 - 0.050737 \cdot x + 0.010137 \cdot x^2 - 0.00075399 \cdot x^3 - 0.000019858 \cdot x^4. \quad (4)$$

Using these two formulas over the full range $1 \leqslant M_V \leqslant 18$ results in the plot shown in Figure 7, which we will use to compare the masses we derive with previously known results. The data in Torres et al. (2010) also permits us to make a fit to

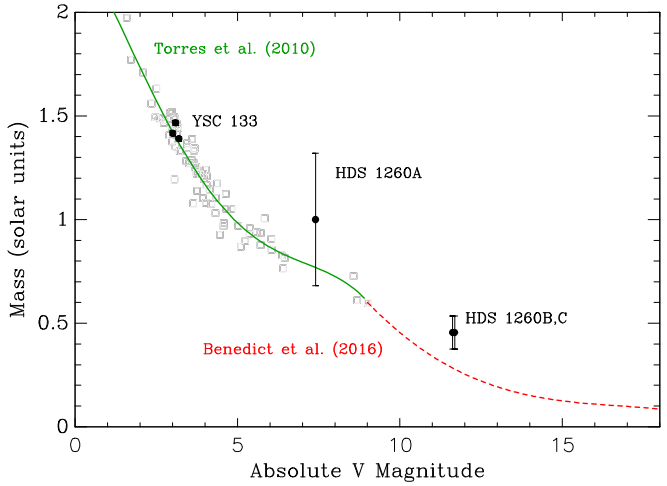

Figure 7. The empirical relation between absolute V magnitude and mass as described in the text. The open squares indicate the original data from Torres et al. (2010) to give a sense of the observational scatter. This relation is used to discuss the systems in this section. Positions of HDS 1260A, HDS 1260B and C (assuming they have equal mass as discussed in the text), and all three components of HD 173093 (YSC 133) are also plotted with their derived uncertainties in mass.

the spectral type; although very approximate, we use that fit as a basic guide in the discussion below.

For HIP 42910, the speckle measures are exclusively at red or near-infrared wavelengths, but the magnitude differences are near 3 for A–BC and between 0.0 and 0.1 for the BC pair. Hipparcos gives a result for the magnitude difference in the H_p filter, which has a center wavelength of 511 nm with a width of 222 nm; that value is 3.53 ± 0.27. Using the apparent magnitude of 10.16 from Hipparcos and the EDR3 parallax of 27.5131 ± 0.0802 mas, we find that the absolute magnitudes of A and BC are likely near 7.40 and 10.90, respectively, where a Δm at V of 3.5 is assumed. Assuming a magnitude difference of zero for BC, we can roughly assign an absolute magnitude to each of those stars of 11.65.

Calling upon Figure 7 to convert these absolute magnitudes to masses, we obtain individual masses and spectral types as follows: $\mathcal{M}_A \approx 0.77\ M_\odot$, a K6V star and $\mathcal{M}_B = \mathcal{M}_C \approx 0.28 M_\odot$, putting both fainter stars near M3V. Thus, from the photometry, we would conclude that the total mass of the triple is approximately $1.33\ M_\odot$. The orbital information and the parallax allow us to determine that the total mass based on the astrometry is $1.90 \pm 0.28 M_\odot$and that the BC pair has a total mass of $0.91 \pm 0.16 M_\odot$. Subtracting these, $\mathcal{M}_A = 1.00 \pm 0.32 M_\odot$, which agrees with the photometric estimate within the uncertainty. Likewise if we assume the B and C components are in fact near-twins, then we can surmise that the individual mass in either of those cases is simply $\mathcal{M}_{B+C}/2 = 0.46 \pm 0.08 M_\odot$. However, in any case, both $\mathcal{M}_A$ and $\mathcal{M}_{B+C}$ are more massive than would be expected based on photometry, and so further observations are warranted; this is a case where very good masses for B and C are within reach in the coming year. The position of these stars on the MLR is shown in Figure 7. Finally, we note that the inclinations of A–BC and BC indicate that the orbital planes of the two components are not aligned; this system may be a useful example in studies of star formation mechanisms as a result.

Turning now to HD 173093, which is another system with near-solar metallicity with $[\mathrm{Fe/H}] = -0.04$ according to Holmberg et al. (2009), we have a composite spectral type of F7V assigned by Houk & Swift (1999). Our orbital analysis in the previous section reveals this to be a trio of F stars of very similar masses in a hierarchical arrangement. The magnitude difference from speckle observations for the AB component is well-determined from five measures using a 543 nm filter, where $\Delta m = 0.62 \pm 0.07$. All measures in this case are due to Tokovinin and his collaborators, e.g., Tokovinin et al. (2016). Using this value together with estimates of the magnitude difference for the Aa,Ab component derived from the spectroscopy, which is 0.1 mag, we can deduce individual absolute V magnitudes for the three stars to be 3.008, 3.092, and 3.192, respectively. Together with the masses, these are used to locate the points on the mass–luminosity relation in Figure 7. We find very good agreement with the curve fitting the Torres et al. (2010) data in all three cases.

5.4. Notes on Four Other Systems

Most of the visual orbits we have calculated are preliminary in nature and their main value at this stage is in providing ephemerides for the coming years for observers to use as a guide while the orbits are further refined for the purpose of obtaining stellar masses. However, there are a handful of systems where a good fraction of the orbit is already traced out by the astrometric data at hand. We give some further information on the systems appearing in Table 4 that have covered at least 270° in position angle in the time since the discovery observation. There are four such systems, all with composite spectral types in the K range. These represent the orbits on the firmest footing at present, and it is worthwhile in these cases to briefly examine the use of the orbit in obtaining mass information. Plots of the orbits of these objects are shown in Figure 8.

5.4.1. HIP 10616=YSC 20

YSC 20, a star suspected of being double based on the observations of the Hipparcos satellite (ESA 1997), was first resolved by our speckle program at the WIYN telescope in 2008 (Horch et al. 2009). SIMBAD shows the composite spectral type to be K0 and the Gaia EDR3 parallax value is 19.65 ± 0.21 mas. Given the apparent V magnitude of 9.41 and using the magnitude difference of 2.63 at 562 nm in Table 3 as a proxy for the ΔV of the pair, we estimate absolute magnitudes for the primary and secondary as 5.99 and 8.62, respectively. Thus, this would appear to be a K0V (or very late G) primary and a late K secondary. Using Figure 7, we estimate masses of 0.88 and 0.66 $M_\odot$, meaning that $\mathcal{M}_{\rm tot} = 1.54 M_\odot$. On the other hand, the Gaia parallax and the orbit we calculate here imply $\mathcal{M}_{\rm tot} = 1.41 \pm 0.07 M_\odot$.

5.4.2. HIP 20745 = WOR 15

Despite the spectral type of K2 shown in SIMBAD, photometry suggests that this pair more likely consists of two mid- or late-K stars of near-equal brightness, with a Δm of 0.25 based on two speckle measures taken at 550 nm. The system is resolved in the Gaia EDR3 catalog (it was not in DR2, nor was a parallax given in that release), and the ΔG shown there is also small and consistent with the speckle result. Using that together with $V = 10.50$ and the EDR3 parallax of 24.1686 ± 0.0878 mas, we arrive at absolute V magnitudes of 8.05 and 8.30. Converting those values to masses, we obtain 0.72 and 0.70 $M_\odot$, and thus a total mass of 1.42 $M_\odot$. The orbital result is $1.32 \pm 0.62 M_\odot$, where the large uncertainty is due mainly to the fact that the semimajor axis is not well constrained by our orbit. Further observations near periastron,

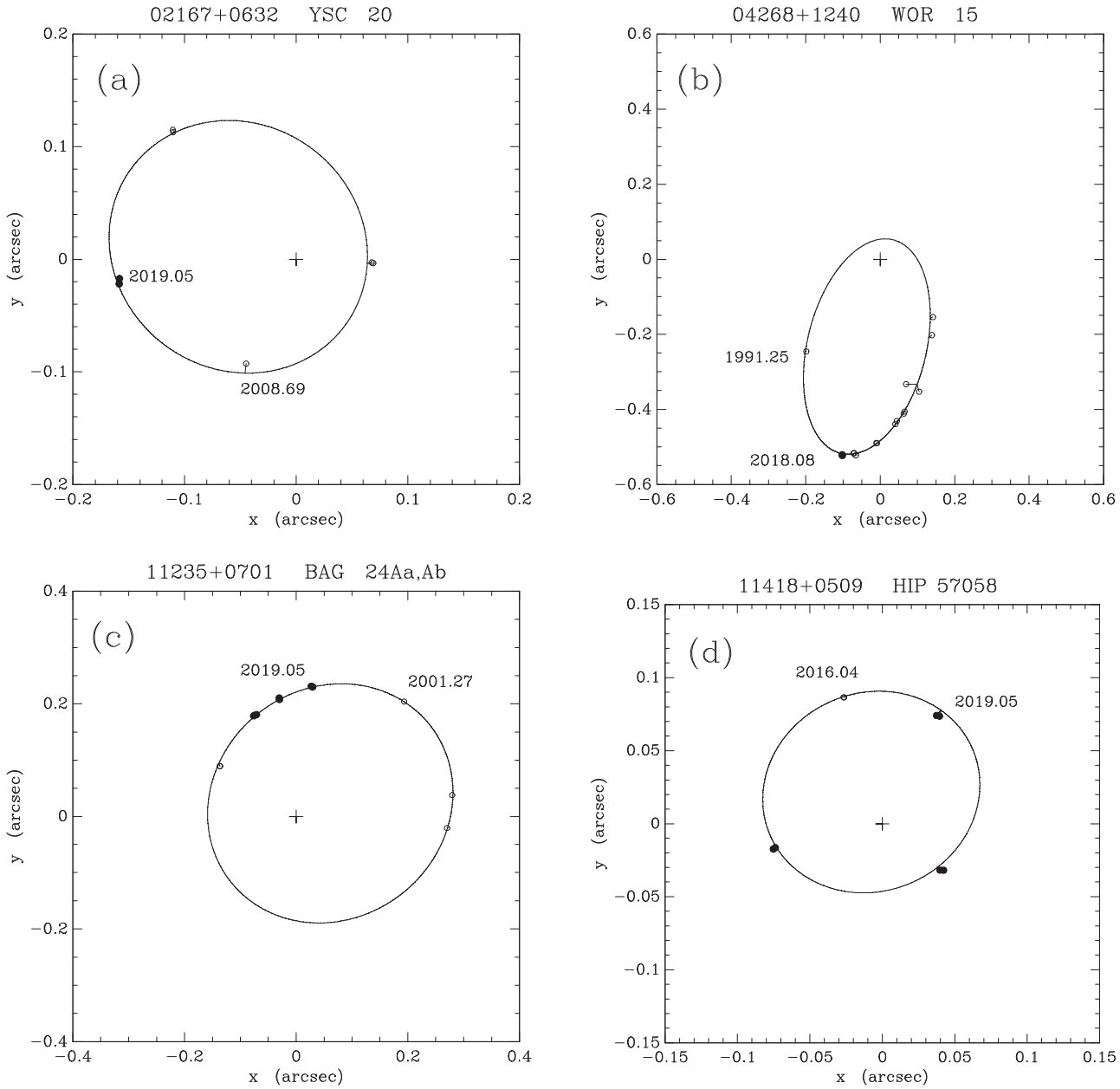

Figure 8. Visual orbits in Table 4 for the four systems in Table 4 with the largest coverage in position angle. (a) HIP 10616 = YSC 20; (b) HIP 20745 = WOR 15; (c) HIP 55605 = BAG 24Aa,Ab; (d) HIP 57058. In all plots, north is down and east is to the right. Measures appearing in Table 3 are shown as filled circles while previous measures listed in the Fourth Interferometric Catalog are drawn as open circles. The cross marks the origin in each case, and line segments are drawn from the ephemeris position on the orbit to each data point.

which will occur in the 2030s, will be important in calculating a definitive orbit of this system. We also note that the EDR3 catalog gives parallax values for both components, and these indicate the two stars are at the same distance within the uncertainties.

5.4.3. HIP 55605 = Bag 24Aa,Ab

First reported in Balega et al. (2006), this system has apparently gone unobserved for over a decade until the first of our observations shown in Table 3. From the 562 nm magnitude difference there and the apparent magnitude and EDR3 parallax, we obtain absolute magnitudes of 7.69 and 9.65. These would suggest photometrically determined masses of 0.75 and 0.50 $M_{\odot}$ using the same method as above, and thus a total mass of 1.25 solar masses. The orbit and distance give a total mass of $1.38 \pm 0.19 M_{\odot}$—excellent agreement at this stage. As with the above system, a later spectral type is implied from the photometry here than exists in SIMBAD (where it shows up as K4V); we estimate K8V and M1V.

5.4.4. HIP 57058

Another pair with a composite spectral type of K4V according to SIMBAD, HIP 57058 was first resolved by our speckle program in 2016 at Gemini-North (Henry et al. 2020). Since that point, we have seen the stars complete nearly a full orbit in the subsequent observations shown in Table 3. Combining the known photometry with the EDR3 parallax result and converting to absolute magnitudes, the primary value is 8.06 and the secondary

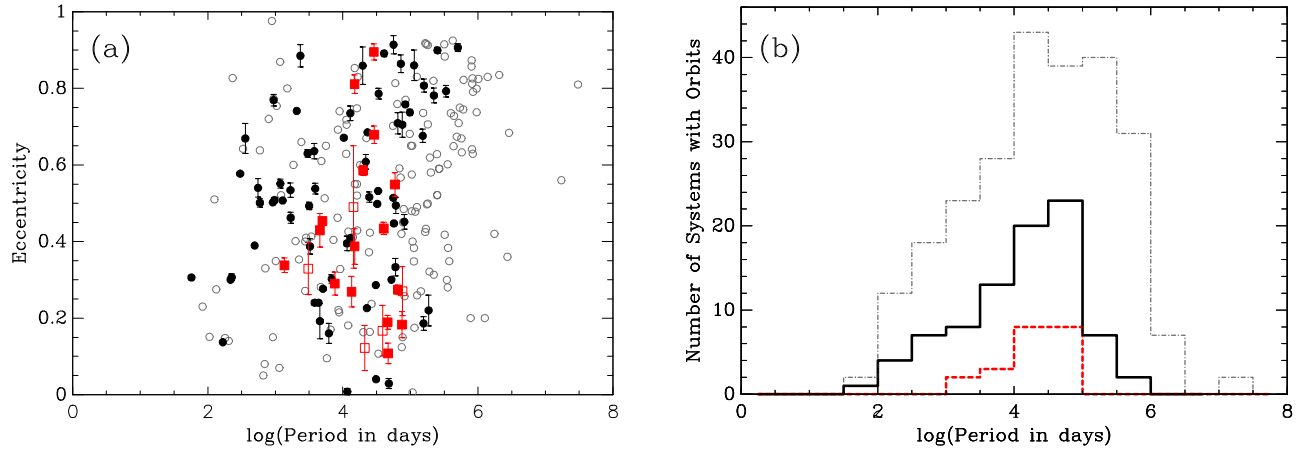

Figure 9. (a) Period–eccentricity diagram for the K stars with known orbits. The orbits in the Sixth Orbit Catalog are shown with circles, and the orbits presented in Table 4 are represented as red squares. If an orbit has an uncertainty in eccentricity of greater than 0.05, then it is shown as an open gray or red symbol. Uncertainties for published orbits in this case are not shown to keep the plot clear. (b) Period histograms for three samples. Here, the dotted–dashed gray histogram corresponds to all systems, the black data set represents those systems with $\delta e < 0.05$, and the red dashed histogram indicates the systems in Table 4.

8.55. These imply a total mass of 1.47 $M_{\odot}$, while the orbit and EDR3 parallax give $1.18 \pm 0.09 M_{\odot}$.

6. Basic Statistics of K-dwarf Visual Binaries

The orbits presented in the previous section consist largely of systems that have a K dwarf as the primary star. In this section, we add our subsample of these objects to the visual orbits previously known and available in the Sixth Orbit Catalog for this spectral type and make a preliminary study of the statistics of the sample. Confining our attention to K dwarfs within 50 pc of the solar system, we find approximately 5000 such objects in current Gaia data. We have cross-identified these objects with those in the Sixth Orbit Catalog, finding a grand total of 225 matches. Six of these objects do not have a complete set of orbital elements, and so discarding those for our purposes here, we are left with 219 previously known orbits. To those, we add the 21 K-dwarf orbits in Table 4, for a grand total of 240 orbits to study. A period–eccentricity relation is shown for these objects in Figure 9(a). It is worth noting that the majority of objects either have no stated uncertainty for eccentricity or have $\delta e > 0.05$. Only 69 previous orbits have $\delta e \leqslant 0.05$, whereas for the new orbits presented here, 16 systems meet that criterion. Therefore, our new sample, shown with data points that are red squares, increases this subsample by roughly 23%.

Two points are of note when studying the appearance of Figure 9(a). First, the period range represented is clearly incomplete; nearly all the orbits plotted have periods between 10^2 and 10^6 days. For a typical K-dwarf binary with a total mass of 1–1.5$M_{\odot}$, these periods correlate to semimajor axes in the range of 0.4–200 au, or given the distances, typical angular values from $\sim 0\farcs1$ to several arcseconds. That is, these are separations easily observable by direct imaging, speckle imaging, and adaptive optics at large telescopes. Outside of these period limits, we anticipate that there are many more binaries; those with shorter periods are being found in our spectroscopic program (Paredes et al. 2021), and those with larger periods would generally not have well-defined orbits due to the small amount of orbital coverage existing in the literature in most cases.

Second, it is interesting to observe that only three systems have an eccentricity less than 0.1 with estimated uncertainty below 0.05, which are HIP 5842, HIP 34025, and HIP 78842, in order of increasing period. The orbit for HIP 5842 is the CD pair of a multiple system (I 27 CD), and the AB pair (HJ 3423AB) has a composite spectral type that indicates that the primary has evolved off the main sequence. Thus, it may not be a particularly good system with which to judge K-dwarf orbital statistics. HIP 34025 (A 1959) has an orbit calculated by Docobo et al. (2006) and only one measure since that time appears in the Fourth Interferometric Catalog. Docobo et al. find an orbital period of 32 yr based on five measures in the fourth quadrant and one (at the time) in the second quadrant. However, the system has a small magnitude difference, and so quadrant determinations should be regarded as provisional. If instead all observations are assumed to be in the same quadrant, then an orbit can be obtained with a 15.5 yr period that appears to fit the data as well as Docobo's but has an eccentricity of 0.76. Until further observations are made of this system, it may be wise to assume that the eccentricity is not as certain as it appears at present. Finally, HIP 78842 (SEE 264AB) is also a quadruple system, with the orbit here representing the middle component in terms of separation; the B component was first resolved in 2008 (Tokovinin et al. 2010) and is now known as WSI 84Ba,Bb, and a 10″ companion (SEE 264AC) is also present. Orbital dynamics that cause the evolution of orbital elements over time may be at play here as well. A group of only four other objects has periods near 1000 days and eccentricities below 0.2, though with substantial uncertainty. These are HIP 1768, 4365, 16192, and 19832. All four are astrometric orbits due to Goldin & Makarov (2007), derived from very small photocenter shifts in Hipparcos data. Eccentricity values above 0.1–0.2 cannot be ruled out in any of these cases. Perhaps Gaia can add to our knowledge here with future data releases, but the available data at present suggest the relative lack of low-eccentricity systems, particularly for periods from at least 10^2–10^4 days.

Figure 9(b) shows a histogram of the same samples as a function of log(period). Here we see that the orbits presented in Table 4 mainly contribute to the period range of 10^4–10^5 days, resulting in a more strongly peaked histogram in that region for systems with well-measured eccentricities. The plot is of course incomplete but points to the possibility of significant improvement through sustained spectroscopic and speckle observing in the coming years, as is our long-term goal.

Finally, in Figure 10, we show the distance histogram of the same three samples: all K-dwarf orbits, those with well-known

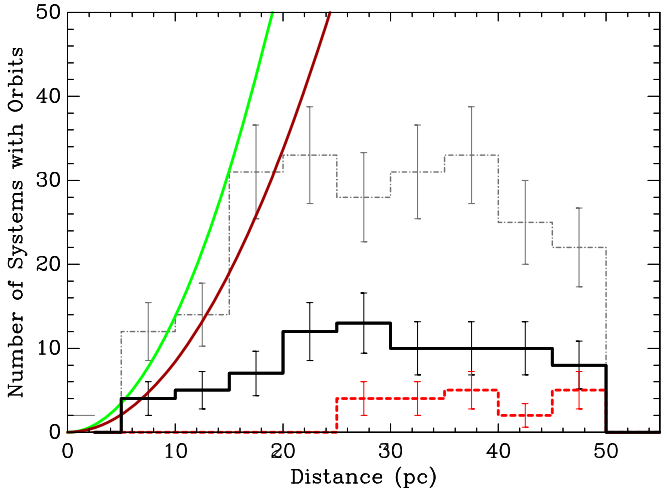

Figure 10. Distance histograms for the full sample of K dwarfs with orbits (shown in the dotted–dashed gray), those orbits with eccentricities with uncertainties of less than 0.05 (represented by the black histogram), and the sample in Table 4 (in dashed red). The green and dark red curves represent the expected number of K-dwarf binaries as a function of distance, making an assumption about the multiplicity rate in each case. For the green curve, the value of 44% is used, which is the known rate for G stars from Raghavan et al. (2010), and for the red curve, we use 26.8%, which is the rate for M dwarfs from Winters et al. (2019).

eccentricities, and our new orbits. If one assumes (1) the RECONS K-dwarf number density of 0.01 per cubic parsec[17] and (2) a multiplicity rate for K dwarfs that is between that for G and M stars, we can begin to estimate how incomplete the current sample is. As discussed above, the sample of visual orbits within 50 pc is mainly limited to the period range of 10^2–10^6 days, and if one examines the period histogram found in Duquennoy & Mayor (1991), then for G dwarfs we find that about half of all objects in their sample have periods falling in this range. So, if we also assume a similar number for K dwarfs and a multiplicity rate like that of G dwarfs, we would predict the number of multiple star systems to follow the green curve in Figure 10. On the other hand, if the rate for M dwarfs is assumed, the dark red curve is obtained. We see from this that the histogram of all known orbits is therefore probably complete or nearly complete to about 20 pc but appears very incomplete at larger distances. A much more robust sample can be made by doing two things. First, it will be important to increase the precision on the known orbital elements for nearby systems paying particular attention to the eccentricity. This would move the black histogram in Figure 10 closer to the gray one. Second, a full reconnaissance of systems beyond 20 pc is needed in order to eventually add many more orbits to the 25 we have presented here. (As seen with the red curve in Figure 10, all of the systems presented here are increasing the previously undetermined sample of orbits for K dwarfs from 25 to 50 pc.) Once these tasks are complete, the statistics of orbital elements of K dwarfs can be fully understood and a meaningful comparison to those with other spectral types can be made.

7. Conclusions

This paper has first provided 378 new speckle observations of 178 binary star systems, taken mainly with the LDT but supplemented with data from WIYN and both Gemini telescopes. We have studied the astrometric and photometric precision of those measures and conclude that they are in line with previous papers in this series. In particular, the estimated uncertainty for the separation measures is 2.07 ± 0.11 mas, and for the position angle, it is of course dependent on the separation, but an average value for the group of measures here is approximately $1\overset{\circ}{.}1$. Photometric precision appears to be on the order of 0.1 mag, as expected for this sample, which mainly consists of stars brighter than $V = 12$.

We used these measures and others in the literature to compute preliminary visual orbits of 25 systems, 21 of which have a K dwarf as the primary star. Two triple systems provided information for mass determinations. First, we had sufficient spectroscopic and speckle observations to compute combined orbits for HD 173093, yielding three high-precision masses of similar F dwarfs of 1.39–1.47 $M_{\odot}$. Second, in the triple system HDS 1260 (HIP 42910), we used the speckle results to determine component masses of 1.00, 0.46, and 0.46 $M_{\odot}$, where these values are larger than anticipated from photometry, indicating that more observations are warranted.

Finally, having identified a sample of 5000 K dwarfs within 50 pc of the solar system using Gaia data, we cross-identified these with existing orbits in the Sixth Orbit Catalog and then added our new orbits to the sample. The period–eccentricity relation for these objects suggests a relative lack of low-eccentricity orbits with the period from 100 to 10,000 days, that is, a range comparable to those of the planets in our own solar system.

E.P.H. gratefully acknowledges support from the National Science Foundation, specifically grants AST-1517824, AST-1616698, and AST-1909560, which allowed all of the SCSU personnel to participate in this work. Likewise, T.J.H. is grateful for NSF grants AST-1517413 and AST-1910130, and G.T.vB. acknowledges support from NSF grant AST-1616084. J.G.W. is supported by a grant from the John Templeton Foundation. The opinions expressed in this publication are those of the authors and do not necessarily reflect the views of the John Templeton Foundation. We thank Paul Klaucke, Richard Pellegrino, and Daniel Nusdeo for their help in obtaining some of the LDT observations, and members of the NASA Ames speckle group for participating in the Gemini observations discussed here. Finally, we acknowledge the contribution of Helmut A. Abt in obtaining the initial spectroscopic observations of HD 173093. Astronomy at Tennessee State University is supported by the state of Tennessee through its Centers of Excellence program.

This work was based in part on observations obtained at the Gemini Observatory, which is operated by the Association of Universities for Research in Astronomy, Inc., under a cooperative agreement with the NSF on behalf of the Gemini partnership: the National Science Foundation (United States), National Research Council (Canada), CONICYT (Chile), Ministerio de Ciencia, Tecnología e Innovación Productiva (Argentina), Ministério da Ciência, Tecnologia e Inovação (Brazil), and Korea Astronomy and Space Science Institute (Republic of Korea). As visiting astronomers to Gemini-N, we are mindful that Maunakea is a sacred space to many native Hawai'ians, and we are grateful for the opportunity to have been present there. Some of the observations in the paper made use of the NN-EXPLORE Exoplanet and Stellar Speckle Imager (NESSI). NESSI was funded by the NASA Exoplanet Exploration Program and the NASA Ames Research Center. NESSI was

[17] http://www.recons.org/census.posted.htm

built at the Ames Research Center by Steve B. Howell, Nic Scott, Elliott P. Horch, and Emmett Quigley. Kitt Peak is home to the Tohono O'odham people, and we are privileged to have been visiting astronomers to that special place.

ORCID iDs

Elliott P. Horch https://orcid.org/0000-0003-2159-1463
Dana I. Casetti-Dinescu https://orcid.org/0000-0001-9737-4954
Todd J. Henry https://orcid.org/0000-0002-9061-2865
Francis C. Fekel https://orcid.org/0000-0002-9413-3896
Matthew W. Muterspaugh https://orcid.org/0000-0001-8455-4622
Daryl W. Willmarth https://orcid.org/0000-0002-4937-7015
Gerard T. van Belle https://orcid.org/0000-0002-8552-158X
Mark E. Everett https://orcid.org/0000-0002-0885-7215

References

Abt, H. A., & Willmarth, D. W. 2006, ApJS, 162, 207
Balega, I. I., Balega, Yu. Yu., Maksimov, A. F., et al. 2006, BSAO, 59, 20
Benedict, G. F., Henry, T. J., Franz, O. G., et al. 2016, AJ, 152, 141
DeRosa, R. J., Patience, J., Vigan, A., et al. 2011, MNRAS, 422, 2765
Docobo, J. A., Tamazian, V. S., Belga, Y. Y., & Melikian, N. D. 2006, AJ, 134, 994
Duchêne, G., & Kraus, A. 2013, ARA&A, 51, 269
Duquennoy, A., & Mayor, M. 1991, A&A, 248, 485
Eaton, J. A., & Williamson, M. H. 2004, Proc. SPIE, 5496, 710
Eaton, J. A., & Williamson, M. H. 2007, PASP, 119, 886
Eggleton, P. P., & Kiseleva-Eggleton, L. 2001, ApJ, 562, 1012
ESA 1997, The Hipparcos and Tycho Catalogs (Noordwijk: ESA)
Fabrycky, D., & Tremaine, S. 2007, ApJ, 669, 1298
Fekel, F. C., & Griffin, R. F. 2011, Obs, 131, 283
Fekel, F. C., Henry, G. W., & Sowell, J. R. 2019, AJ, 158, 189
Fekel, F. C., Rajabi, S., Muterspaugh, M. W., & Williamson, M. H. 2013, AJ, 145, 111
Fekel, F. C., Tomkin, J., & Williamson, M. H. 2009, AJ, 137, 3900
Fitzpatrick, M. J. 1993, in ASP Conf. Ser. 52, Astronomical Data Analysis Software and Systems II, ed. R. J. Hanish, R. V. J. Brissenden, & J. Barnes (San Francisco, CA: ASP), 472
Gaia Collaboration 2018, A&A, 616, A1
Gaia Collaboration, Smart, R. L., Sarro, L. M., et al. 2021, A&A, 649, A6
Goldin, A., & Makarov, V. V. 2007, ApJS, 173, 137
Griffin, R. F. 2013, Obs, 133, 269
Hartkopf, W. I., Mason, B. D., & Worley, C. E. 2001a, AJ, 122, 3472
Hartkopf, W. I., McAlister, H. A., & Mason, B. D. 2001b, AJ, 122, 3480
Henry, T. J., Nusdeo, D. A., Horch, E. P., et al. 2020, AJ, submitted
Hoffleit, E. D., & Jaschek, C. 1982, The Bright Star Catalog (4th ed.; New Haven, CT: Yale Univ. Observatory)
Holmberg, J., Nordström, B., & Anderson, J. 2009, A&A, 501, 941
Horch, E., Dinescu, D., Gerard, T., et al. 1996, AJ, 111, 1681
Horch, E., Veillette, D., Gallé, R., et al. 2009, AJ, 137, 5057
Horch, E. P., Casetti-Dinescu, D. I., Camarata, M. A., et al. 2017, AJ, 153, 212
Horch, E. P., Gomez, S. C., Sherry, W. H., et al. 2011, AJ, 141, 45
Horch, E. P., van Belle, G. T., Davidson, J. W., Jr., et al. 2020, AJ, 159, 233
Houk, N., & Swift, C. 1999, Michigan Catalogue of Two-dimensional Spectral Types for the HD Stars, Vol. 5 (Ann Arbor, MI: Univ. Michigan)
Kordopatis, G., Gilmore, G., Steinmetz, M., et al. 2013, AJ, 146, 134
Kozai, Y. 1962, AJ, 67, 591
Lacy, C. H. S., & Fekel, F. C. 2011, AJ, 142, 185
Lidov, M. L. 1962, P&SS, 9, 719
Lindegren, L., Klioner, S. A., Hernández, J., et al. 2021, A&A, 649, A2
Lohmann, A. W., Weigelt, G., & Wirnitzer, B. 1983, ApOpt, 22, 4028
MacKnight, M., & Horch, E. P. 2004, BAAS, 36, 788
Mason, B. D., Wycoff, G. L., Hartkopf, W. I., et al. 2001, AJ, 122, 3466
Mazeh, T., & Shaham, J. 1979, A&A, 77, 145
Meng, J., Aitken, G., Hege, K., & Morgan, J. 1990, JOSAA, 7, 1243
Muterspaugh, M. W., Hartkopf, W. I., Lane, B. F., et al. 2010, AJ, 140, 1623
Muterspaugh, M. W., Lane, B. F., Fekel, F. C., et al. 2008, AJ, 135, 766
Muterspaugh, M. W., Mijngaarden, M. J. P., Henrichs, H. F., et al. 2015, AJ, 150, 140
Nidever, D. L., Marcy, G. W., Butler, R. P., Fischer, D. A., & Vogt, S. S. 2002, ApJS, 141, 503
Paredes, L. A., Henry, T. J., Jao, W., et al. 2021, BAAS, 53, 332.02
Raghavan, D., Mcalister, H. A., Henry, T. J., et al. 2010, ApJS, 190, 1
Scarfe, C. D. 2010, Obs, 130, 214
Scott, N. J., Howell, S. B., Horch, E. P., & Everett, M. E. 2018, PASP, 130, 054502
Tokovinin, A., Mason, B., & Hartkopf, W. 2010, AJ, 139, 743
Tokovinin, A., Mason, B. D., Hartkopf, W. I., Mendez, R. A., & Horch, E. P. 2015, AJ, 150, 50
Tokovinin, A., Mason, B. D., Hartkopf, W. I., Mendez, R. A., & Horch, E. P. 2016, AJ, 151, 153
Tokovinin, A., Thomas, S., Sterzik, M., & Udry, S. 2006, A&A, 450, 681
Torres, G., Andersen, J., & Giménez, A. 2010, A&ARev, 18, 67
van Leeuwen, F. 2007, A&A, 474, 653
Wenger, M., Ochsenbein, F., Egret, D., et al. 2000, A&AS, 143, 9
Willmarth, D. W., Fekel, F. C., Abt, H. A., & Pourbaix, D. 2016, AJ, 152, 46
Winters, J. G., Henry, T. J., Jao, W.-C., et al. 2019, AJ, 157, 216